X-ray Ionization and the Influence of Magnetic Fields on the Growth of Gas Giant Planets

Senior Thesis by

Stacy Kim

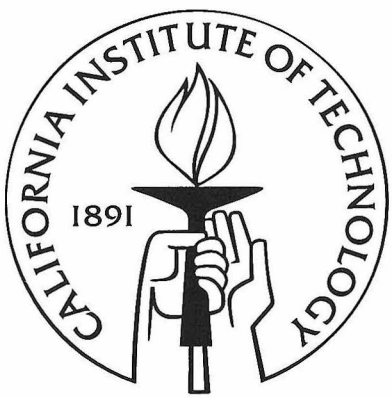

California Institute of Technology

Pasadena, California

2013

(Submitted May 7, 2013)

© 2013
Stacy Kim
All Rights Reserved

Acknowledgments

This project marks the last in my undergraduate career, as well as the last I'll have done during that time with my advisor, Neal Turner, with whom I have worked for with two years. Two years is a long time, and with someone as patient and committed as Neal, the list of things I am thankful for has grown quite long. In particular, I'd like to thank him for understanding when the academic workload became tough; giving me a non-Caltech perspective on doing astrophysics; for the many stimulating discussions on a broad variety of topics concerning protoplanetary disks and planet formation; for giving me my first true taste of how progress is made at the frontiers of astrophysics; and for giving me a chance to try computational work, which I hope to continue during my graduate career. I'd also like to thank him for all the trips he made from JPL to collaborate with me at Caltech.

The things I've learned while working with him has, I hope, laid the foundations for a career in astrophysics – the realization that one can find explanations for even the smallest oddities in my results; to perform quick, back-of-the-envelope estimates to speed error checking, evaluate conjectures, and interpret results; that communicating technical material is much like telling a story; and demonstrating that science can be more than a job, and more like an enjoyable hobby which one has the happy fortune of being paid for. I have not mastered many of these skills yet, and am sure I will come back to the things I've learned from him again and again.

Most of all, I'd like to thank him for his encouragement, which has convinced me to stay in the field and rekindled my passion for astrophysics when the pace of academics at Caltech had worn me out. It has been a privillege and a pleasure to work with Neal, and his patience and efforts will not be easily forgotten. I am sure I will continue to discover the benefits of having worked with him for many years in the future.

Lastly, we would like to thank Satoshi Okuzumi (Tokyo Tech) for supplying a routine to calculate the primary x-ray absorption opacities used in this study as well as Barbara Ercolano (University Observatory Munich) for providing advice concerning x-ray transfer.

Abstract

The past two decades have witnessed an explosion in the number of known planets outside our Solar System. The exoplanets' number and diversity are surprising, with many planetary systems quite unlike our own. Naturally, the question of their origins arise. Yet our knowledge of how planetary systems form and evolve are far from complete, and even for our own Solar System, many fundamental questions remain. One puzzle concerns the formation of gas giants with masses intermediate between Jupiter ($M_J = 320M_\oplus$, where $M_\oplus = 6 \times 10^{27}$ g equals the mass of the Earth) and Neptune ($M_N = 17M_\oplus$), which our Solar System provides a prime laboratory for study: Saturn ($M_S = 95M_\oplus$). According the popular core accretion scenario, gas giants form through the growth of an ice and rock core that, upon becoming sufficiently massive, accretes a gaseous envelope from the surrounding protoplanetary disk. If the mass of the envelope reaches the mass of the core, runaway gas accretion commences, with terminal masses typically a Jupiter mass or more. The combined mass of the envelope and core at the critical point when runaway accretion begins is about a Neptune mass. Saturn, being a factor of a few times more massive than Neptune, achieved this critical mass, yet appears not to have undergone runaway accretion to an extent similar to Jupiter, posing a problem for the core accretion hypothesis.

In this thesis, we investigate one possible explanation for Saturn's low mass: magnetic fields. If the gas surrounding a protoplanet is sufficiently ionized, it can be well coupled to the ambient magnetic field; as magnetized gas accretes onto the protoplanet, magnetic pressure and tension forces would grow, prematurely halting the flow of gas. To investigate this possibility, a preexisting Monte Carlo transport code was extended to calculate x-ray transfer. The code was applied to calculate ionization rates for a proto-Saturn still embedded in the protosolar disk. The results were inputted into a simplified chemical reaction network, which takes into account recombination and charge transfer and returns the ionization fraction of the disk. Magnetic diffusivities in proto-Saturn's vicinity can then be calculated, allowing us to infer whether the magnetic field was coupled well enough to the gas surrounding proto-Saturn to affect gas dynamics.

We find that for a disk depleted in small grains and possessing magnetic fields of about 0.1 G, magnetic fields were likely well-coupled to the gas near proto-Saturn and may have influenced its gas accretion rate.

Contents

List of Figures

Overview

A summary of the current state of affairs regarding the formation of gas giant planets by core accretion and the possible role that magnetic fields could have are first discussed in Chapter 1. I then give an detailed overview of the relevant physics involved in evaluating the role of magnetic fields in the formation of gas giants. The complex geometry of the protostellar disk preclude much progress on the subject by way of analytical means, and thus the relevant physics must be studied numerically. Therefore where relevant, the pertinent numerical methods and considerations are presented. In Chapter 2, I discuss the ionization of protostellar disks, introduce the radiative transfer code that provided the backbone for most of the analysis performed in this thesis, and describe how I extended the code to calculate x-ray ionization rates. I then describe the chemical kinetics that determine the disk's final ionization state, the associated numerics required to solve the kinetic equations, and explain how the coupling of the magnetic field to the gas can be determined from the results in Chapter 3. The physics and numerical tools introduced in these chapters are finally applied to the formation of Saturn in Chapter 4, in which the results are presented and their implications outlined. The thesis is summarized in Chapter 5.

Chapter 1

Introduction

1.1 The Formation of Gas Giants

The question of how planets and the Solar System formed has engaged thinkers as early as the seventeenth century, yet a single compelling theory has remained elusive even to the present day. The frameworks of such a theory, however, are in place. It is believed that the origins of the planets date back to the formation of their host star, which form when a dense cloud of molecular gas collapses under its own gravity. The parent cloud typically has excess angular momentum for it to directly collapse into a star, which can in part be resolved by the formation of a disk.

In the quasi-stable environment of the disk, small, submicron interstellar grains can gradually grow through collisions with other grains in a process that accelerates as the solidy body grows in mass. This process halts when the surrounding supply of solids is depleted. If the solid body is embedded in a substantial gaseous environment, it can continue to accumulate mass by accreting the surrounding gas. During this phase of growth, the gaseous envelope can support itself against the gravitational pull of the core. The gas accretion rate is primarily dependent on how quickly the envelope can radiate away the accretion energy from the planetesimals it accretes; the faster the envelope can radiatate away its heat, the faster it can shrink and new material can enter the protoplanet's gravitational reach (also known as the Hill sphere). Also important are the mass of the core, which determine the extent of its Hill sphere, and the abundance of planetesimals. When the mass of the envelope reaches the mass of the core, the self-gravity of the envelope becomes significant, and the addition of mass causes the envelope to shrink, leading to runaway gas accretion. The runaway growth terminates when the surrounding supply of gas is depleted. This can occur when the planet's Hill sphere reaches the vertical scale height of the disk, at which point the planet's tidal interactions with the disk halts the flow of gas towards the planet, or the disk disperses, which typically occurs on a timescale of 2-5 $\times 10^6$ yr (for a more detailed overview of the formation of gas giants, see Lissauer & Stevenson (2007)).

Pollack et al. (1996) was the first to self-consistently model the evolution of a gas giant. In

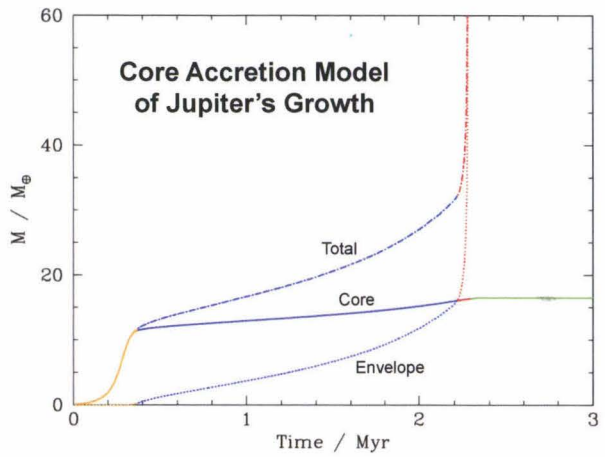

Figure 1.1: Mass evolution of proto-Jupiter under the core accretion scenario. There are three distinct phases of growth: the formation of a solid core, followed by a long period of slow hydrostatic growth during which a gaseous envelope begins to form, which gives way to gas runaway accretion once the envelope mass equals the core mass. The length of the hydrostatic growth phase is determined by how efficiently the envelope can contract, which is dependent on the amount of solid bodies accreted (which heats the envelope as it releases its gravitational potential energy) and the opacity of the envelope.

their simulations of the formation of Jupiter, they found that the growth of a solid core occured in about 5 $\times 10^5$ years, followed by a 7 $\times 10^6$ year period of slow hydrostatic growth that concluded with a comparatively short phase of runaway gas accretion. During the hydrostatic growth phase, the combined mass of the core and envelope was about a Neptune mass. Follow up studies varying the opacity of the envelope (Hubickyj et al., 2005, see Figure 1.1), which sets the efficiency of radiative cooling, or incorporating radial migration in the disk, which resupplies the protoplanet with planetesimals and thus accelerates growth, have achieved the formation of Jupiter within the disk dispersal time. Moreover, when the Hill radius of proto-Jupiter becomes comparable to the vertical scale height of the disk and gas accretion halts, it achieves a mass similar to its observed mass.

An attempt to explain the formation of Saturn in a similar manner fails to reproduce its observed mass. Saturn, being a few times more massive than Neptune, also reached the critical mass required for the onset of runaway gas accretion. If Saturn's runaway growth phase ended when its Hill sphere filled the vertical dimension of the protosolar disk, Saturn could also have achieved a mass similar to Jupiter's. The chances that the disk dissipated while Saturn was undergoing runaway growth are highly unlikely; the duration of the runaway growth phase would have been at most 10^4 years, a small fraction of the lifetime of the disk. The disk dispersial timescale may also be short; photoevaporation, for example, would clear the disk in a matter of 10^4 or 10^5 years. That these two brief events would overlap within the protostellar disk's lifetime seems unlikely.

The inadequacy of the core-accretion model in explaining how a Saturn-mass planet forms is further underlined by the discovery of Saturn-mass planets around many sun-like stars Howard et al. (2012). It appears that the formation of Saturn-mass planets could not have been a coincidence event and an alternative explanation is required to explain why Saturn did not complete runaway accretion.

1.2 The Influence of Magnetic Fields

It has been well established that magnetic fields have an important effect on the evolution of solid bodies and the formation of planets in the protoplanetary disk. Young stars have been observed to have surface field strengths on the order of kiloGauss (Johns-Krull 2007), but field strengths drop dramatically with distance from the star. Bai & Goodman (2009) calculate a lower bound for the RMS field strength in the disk assuming a minimum-energy magnetic configuration in which the ratio between the field's radial and toroidal components only slightly differ from the fastest growing mode of the magnetorotational instablity (MRI), given by the relation

$$B = 3.2\dot{M}_{-7}^{1/2} r_{AU}^{-11/8} \text{ G}, \tag{1.1}$$

where $\dot{M}_{-7}$ is the mass accretion rate in units of 10^{-7} $M_\odot$ yr^{-1}, and r_{AU} is the distance from the protostar in units of AU. A typical mass accretion rate of $\dot{M} = 10^{-8}$ $M_\odot$ yr^{-1} yields a minimum magnetic field strength of about 0.04 G at the distance of Saturn.

While the fields in the disk are small, they can still play an instrumental role by aiding the development of various instabilities that have significant consequences for disk evolution. A celebrated example is the MRI, an important angular momentum transport mechanism that can reproduce the observed accretion timescales of protostellar disks. Such instabilities may also help drive or inhibit gas accretion onto gas giants.

Chapter 2

X-ray Transfer

2.1 X-ray Ionization

2.1.1 Sources of ionization

In the protostellar context, there are three main sources of ionization: radioactive decay, cosmic rays, and stellar x-rays. Ionization due to radioactive decay is primarily caused by the decay of the short-lived nuclide ^{26}Al (which has a half life of 0.72 Myr), at the initial rate $\zeta = 2.6 \times 10^{-19}$ s^{-1} per hydrogen molecule, assuming solar abundances. The rate would vary based on the amount of radioactive material seeded into the disk when it formed, the age of the disk, and whether the decay sources have been integrated into solid bodies large enough to absorb the breakdown products internally.

Armitage (2010) calculates the ionization rate due to cosmic rays to be

$$\zeta = 10^{-17} \exp\left[-\Delta\Sigma/\Sigma_{stop}\right] \text{ s}^{-1}, \tag{2.1}$$

where $\Delta\Sigma$ is the column density measured from the top of the disk and $\Sigma_{stop} = 10^2$ g cm^{-2} (Umebayashi & Nakano, 1981). This is an upper limit to the cosmic ray ionization rate as the stellar winds of young stars may be able to exclude some or all of the cosmic ray flux.

The remaining ionziation source is thus stellar x-rays. Young stars emit most of their energy in the optical and infrared. X-ray energies are thus in the Wien limit of a protostellar blackbody, in which the emitted flux falls exponentially with increasing photon frequency. A protostar would thus would emit few x-rays. However, magnetic reconnection in the corona around a protostar can generate plasmas hot enough to emit x-rays via thermal bremsstralung radiation. Turner & Sano (2008) provided a fit to the ionization rate due to an x-ray source described in Igea & Glassgold (1999, hereafter IG99), in which the source was represented as twin rings of radius 10 $R_\odot$ located 10 $R_\odot$ above and below the disk midplane. For a source with a temperature of 5 keV and luminosity

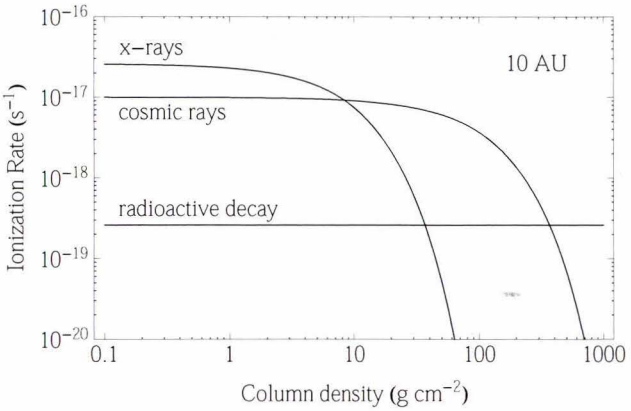

Figure 2.1: Ionization rates in the protosolar disk due to x-rays from the solar corona, cosmic rays, and radiative decay at 10 AU, the distance of Saturn.

$L_X = 2 \times 1{-}^{30}$ erg s^{-1}, the ionization rate in the disk is given by

$$\zeta = 2.6 \times 10^{-15} r_{AU}^{-2} \exp\left[-\Delta\Sigma/\Sigma_{stop}\right] \text{ s}^{-1}, \tag{2.2}$$

where $\Sigma_{stop} = 8$ g cm^{-2}. At the distance of Saturn, this would amount to an ionization rate of 2.6×10^{-17} s^{-1} at the top of the disk, a factor of a few times greater than the cosmic ray ionization rate and substantially greater (by a couple orders of magnitude) than the radionuclide rate.

2.1.2 The x-ray source: thermal bremsstrahlung radiation

The thermal bremsstrahlung spectrum of a plasma is well approximated by

$$L(E) = \frac{L_X}{kT_X} \frac{1}{E} \exp\left[-E/kT_X\right], \tag{2.3}$$

where T_X is the temperature of the plasma. A less approximate treatment requires corrections derived from quantum electrodynamics; we briefly note the effects due to such a correction here. For an ionized, isothermal plasma, we can assume it is composed of charged particles with a velocity following the Maxwell distribution. The emissivity of such a plasma is given by

$$\varepsilon_\nu^{ff} = \frac{2^5 \pi e^6}{3mc^3} \left(\frac{2\pi}{3km}\right)^{1/2} T^{-1/2} Z^2 n_e n_i e^{-h\nu/kT} \bar{g}_{ff}(T, \nu)$$

where $\bar{g}_{ff}$ is the velocity averaged Gaunt factor, derived from quantum electrodynamics. For the photon energies and electron temperatures in question, $\bar{g}_{ff}$ is within a factor of 5 of unity, and the net effect is to increase the energy output at low frequencies and decrease the output at high frequencies. Since the albedo of low energy x-rays is low while the albdeo of high energy x-rays is high, this results in higher ionization rates in the thin outer skin of the disk and lower ionization in the disk interior. As in IG99, we approximate $\bar{g}_{ff} = 1$, thereby neglecting the effect of this factor.

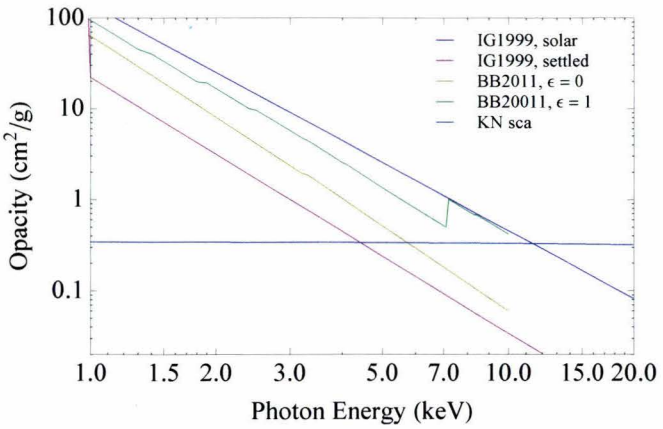

Figure 2.2: Scattering and absorption opacities used in this study. The horizontal line denotes the scattering opacity derived from the Klein-Nishina formula. The absorption opacities, from top to bottom, are (1) IG99's power-law fit assuming solar abundances, (2) Bethell & Bergin (2011)'s more detailed fit assuming no settling of dust and (3) complete settling of dust, and (4) IG99's power-law fit assuming a solar abundance but with heavy elements settled onto grains.

2.1.3 Effects of disk geometry

One can derive a rough estimate for the ionization rate due to x-rays at the vicinity of the proto-Saturn through Equation 2.2. For the protosolar disk, the surface density at 10 AU would be about 54 g cm^{-3}, giving an ionization rate of 3×10^{-20} s^{-1}, lower than the rate due to cosmic rays.

There are several reasons to suppose that the x-ray ionization rates at the midplane may be higher than this simple estimate suggests. The proto-Saturn was sufficiently massive for the torques it exerts on the protosolar disk to open a gap of reduced density surrouding its orbit. The gap can increase the flux of x-rays into the midplane of the disk in several ways. The removal of material in the gap exposes the outer rim to direct stellar irradiation, which causes the rim to heat up and expand in height, which allows the rim to intercept more photons. The build up of material at the outer edge of the gap also increases the chance that x-rays scattered (or absorbed) in the rim. X-rays scattered in the rim have an accentuated probability of being scattered directly backwards – deeper into the gap – or forwards (see Figure 2.3b for the x-ray scattering phase function), thereby increasing the flux of ionizing x-rays at the midplane.

2.2 Numerics: Monte Carlo X-ray Transfer

The complex geometry of the protostellar disk necessitates the use of numerical methods in deriving the disk's ionization profile. I thus now turn to a discussion of numerical x-ray transfer. A pre-existing radiative transfer code for protostellar disks written by N. J. Turner (e.g. Turner et al. (2012), described below in 2.2.1) was extended to calculate the transfer of x-rays following the methodology of IG99. The details of the procedure are outlined in 2.2.2, and the tests performed to check whether the procedures in IG99 had been implemented correctly is discussed in 2.3.

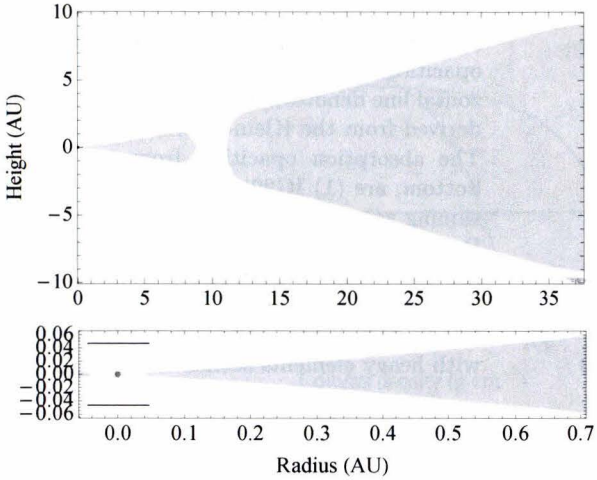

(a) Schematic of disk and x-ray source

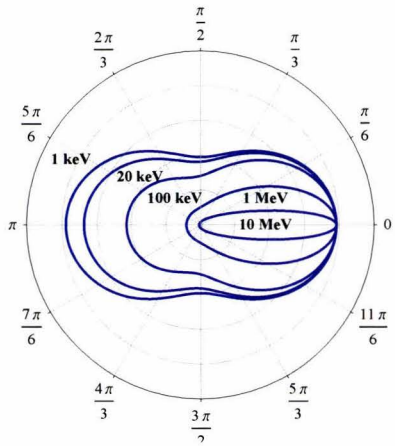

(b) The Klein-Nishina phase function

Figure 2.3: (a) The setup of the disk for x-ray transfer (axes are in units of AU). At bottom is a close-up of the central disk showing the x-ray sources (the double horizontal bands), the central star, and the disk, to scale. The x-ray sources consist of two rings of radius 10 $R_\odot$ centered on the symmetry axis at a height $10R_\odot$ above the midplane. The minimum mass solar nebula, the disk model studied in IG99 and also modeled here (e.g. see Fig. 2.4) in order to validate implementation of x-ray transfer, is similar except without the gap. (b) The Klein-Nishina phase function, which gives the probability that a high-energy photon scattering off a free electron scatters into a given angle.

2.2.1 Monte Carlo radiative transfer

The 2D Monte Carlo radiative transfer code written by N. J. Turner was orignally written to calculate the optical and infrared transfer of protostellar emission in a passive disk. The code solves the equation of radiative transfer, which is given by

$$\frac{\partial I_\nu}{\partial s} = -\epsilon_\nu \rho (I_\nu - S_\nu) \tag{2.4}$$

where ∂s is the distance traveled by a beam of light of frequency ν with intensity I_ν traveling through a medium with extinction ϵ_ν and a source function S_ν. The source function is given by

$$S_\nu = \frac{\kappa_\nu B_\nu(T) + \sigma_\nu J_\nu}{\kappa_\nu + \sigma_\nu} \tag{2.5}$$

where B_ν is the Planck function, κ_ν the mass absorption coefficient, σ_ν the mass scattering coefficient, and J_ν is the mean intensity at ν.

The code requires as inputs the disk surface density profile, the grain model (which determines the disk opacity), and stellar parameters (its effective temperature and radius). The disk is often assumed to be axisymmetric for computational expedience. The protostellar luminosity is divided into a given number of monochromatic photon packets (typically 10^5 to 10^8). Each packet is assigned a frequency with a probability drawn from the protostellar blackbody spectrum, and is followed

from its emission at the central protostar through it's ensuing scattering, absorption, and reemission in a dusty disk until it escapes the computational domain. Assuming that the dust is in local thermodynamic equilibrium, packets are reemitted according to an immediate reemission procedure by Bjorkman & Wood (2001) in which the packet's energy is added to its surroundings and then reemitted with its original energy but with a frequency chosen from the difference spectrum of the local temperature before and after the packet is absorbed. Thus as more photons are passed through the disk, the disk temperatures relax to the correct solution, eliminating the need for CPU-costly iteration required otherwise. Absorption is treated as a continuous process as prescribed by Lucy (1999), which reduces the noisiness inherent to Monte Carlo sampling and accounts for possible contributions a packet could have made as it travels through the disk. At the end of the simulation, the temperature and density profile of the modeled disk is obtained.

The vertical structure of the disk is determined by the balance of gravitational and pressure (supplied by the gas thermal energy) forces, i.e. hydrostatic equilibrium, and is thus modified by disk heating. Modifications to the disk density profile in turn can affect the amount of starlight it absorbs. Thus to obtain a self-consistent temperature and density profile, vertical hydrostatic equilibrium is recalculated following radiative transfer. This two-step process can be iterated until solutions converge, which generally takes about 5 iterations.

2.2.2 Modifications for x-ray transfer

The Monte Carlo code was extended for computing x-ray transfer according to the scheme outlined in IG99. Three main modifications were made. Firstly, x-ray are not emitted at the protostar but in the protostellar corona, which IG99 represented as two rings of radius 10 $R_\odot$ located 10 $R_\odot$ above and below the plane of the disk and centered on the symmetry axis, representing the helmet-streamer reconnection surface (see Figure 4.4).

The second modification stemmed from differences in the desired result for optical/infrared vs. x-ray transfer. The amount of heat transferred by a particular photon is dependent on the local temperature of the disk, which depends on the energies of the photons that have locally passed through. In comparison, ionization rates due to x-rays of different energies are independent of each other. Thus instead of pre-specifying a spectrum of frequencies to sample as must be done in optical/infrared transfer, the source spectrum can be constructed by running a series of monochromatic Monte Carlo transfer calculations for a set of source x-ray energies, then weighting the the resulting set of monochromatic ionization rates according to the desired source spectrum. Moreover, local ionization rates depend on the local x-ray mean intensity, which can be obtained in a single (non-iterative) Monte Carlo calculation.

Lastly, the disk x-ray opacity differs from its optical/infrared opacity. X-rays are scattered non-isotropically by free electrons with a cross section and phase function given by the Klein-Nishina

formula. Additionally, it was assumed that when x-rays are absorbed, their energy is entirely consumed in excitations and in ionizing the disk, and thus were not reemitted. A few different absorption cross sections were variously adopted, including simple power-law fits used in IG99 and a more detailed version fitted by Bethell & Bergin (2011) (see Figure 4.4 for a plot of the different opacities used in this study). One can see that the albedo

$$\alpha_\nu = \frac{\sigma_\nu}{\sigma_\nu + \kappa_\nu}$$

where σ_ν and κ_ν are the scattering and absorption coefficients at the frequency ν, respectively, increases dramatically as photon energies increase. Thus the deeper one goes into a disk, ionization is due increasingly to higher energy x-rays.

For each cell in the grid, the spectrum of x-ray mean intensities was stored in 60 bins (indexed here by k) spanning 1 to 20 keV. The x-ray ionization rates were then computed from the relation

$$\xi_{mn} = \sum_{k=1}^{60} \frac{J_{mn}(E_k)\sigma(E_k)}{\Delta\epsilon}$$

where the indices m and n denote the grid coordinates of a particular cell, J_{mn} denotes the mean intensity, σ the absorption cross section, and $\Delta\epsilon = 37eV$ the average energy required to form an ion pair, accounting for the various species involved and energy losses due to excitation. The Monte Carlo code was modified to execute this procedure for repeated for multiple monochromatic sources given a disk and x-ray source model. Assembly of the total ionization rates due to a source emitting thermal bremsstrahlung radiation was implemented in a separate program called `ionize`.

2.3 Tests

2.3.1 Normalized ionization rates

To verify that x-ray transfer had been implemented correctly, ionization rates were calculated at 1 AU for the protosolar disk (i.e. the minimum mass solar nebula, or the MMSN, which essentially derives a lower bound for the mass of the protosolar disk by smoothing the masses of the planets into a continuous distribution and adding gas believed to have been lost at the end of the disk's lifetime) and the results compared to those calculated in IG99 (see Figure 2.4). Initial implementation of the x-ray transfer procedure produced ionization profiles that shared the same features as those calculated in IG99, such as greater penetration depths and scattering shoulders for higher energy x-rays, but ionization rates were lower by nearly two orders of magnitude for lower energy x-rays and about a factor of $\sim$20 for higher energy x-rays.

Key sources of error were found in the calculation of the mean intensities. Firstly, it was dis-

covered that the expressions involving the mean intensity in IG99 (eqns 18 and 19) were missing a missing factor of 4π. The second modification involved the algorithm used to calculate mean intensities. The radiative transfer code originally calculated mean intensities according to an algorithm outlined in Lucy (1999), which essentially integrated over the paths traveled by photon packets:

$$J_{mn}(\nu)d\nu = \frac{1}{4\pi}\frac{E_\gamma}{\Delta t}\frac{1}{V_{mn}}\sum_{d\nu}\ell_{mn}$$

In comparison, mean intensities were calculated in IG99 by computing the effective cross-sectional area of each cell:

$$J_{mn}(\nu)d\nu = \frac{1}{4\pi}\frac{n_{mn}(\nu)E_\nu}{\langle A_{nm}\rangle}$$

where n_{nm} is the number of packets that passed through cell n, m with an estimated cross-sectional area $\langle A_{nm}\rangle$. While the method used in IG99 produced ionization rates that agreed to within a factor of at most 1.6-1.7 at low energies and matched those calculated by IG99 at higher energies better than those calculated using Lucy (1999)'s method, the latter is slightly faster, taking as low as 75% of the time required for the former.

2.3.2 Ionization rates for a thermal x-ray spectrum

As a last check, we calculated ionization rates assuming a thermal x-ray source spectrum of luminosity L_X and at various temperatures for the MMSN model at 1 AU, and compared them to the results obtained by IG99. Again, we found that our ionization rates shared similar features as those calculated by IG99, but the rates we calculated were higher by a factor of 2-3, possibly indicating a difference in how we weighted each of the monochromatic ionization rates to assemble the total rate.

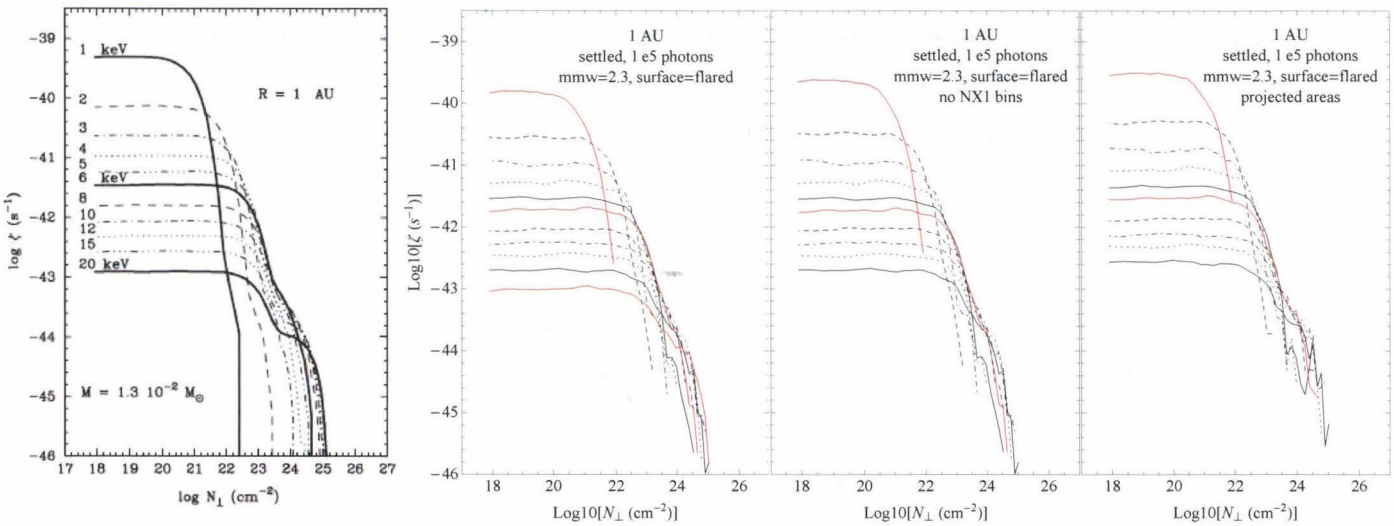

(a) Igea & Glassgold (1999) (b) J via Lucy (1999). (c) Direct calculation of rates. (d) J via projected areas.

Figure 2.4: Ionization rates computed in IG99 and by `ionize`. The line styles between the two figures correspond except that the black and dashed-doubled-dotted lines on the figure at left correspond to the red and black lines on the figure at right, respectively (note that the 20 keV line is missing in (b) and (c)). The scattering shoulder that appears for higher energy x-rays occurs due to the high albedos at such energies (see Figure 2.3). Features such as the penetration depth and scattering shoulders match between IG99 and `ionize`; the absolute ionization rates, however, are consistently lower, with greater discrepancies at lower energies. (a) Ionization rates calculated by IG99 for the MMSN at 1 AU, assuming that the gas is of solar elemental abundance but depleted in heavy elements (settled onto grains). (b) Ionization rates calculated by computing mean intensities integrating over photon paths as prescribed by Lucy (1999). (c) Same as in (b), but instead of binning mean intensities and computing ionization rates by assuming a single frequency for all contributions in each bin, the exact photon frequencies were used to compute ionization rates. This increased the ionization rate by as much as 50%. (d) Ionization rates computed using the algorithm used in IG99 for computing mean intensities, which uses projected areas instead of integrating over a photon's path as recommended by Lucy (1999). Scattering shoulders are more distinct as in IG99.

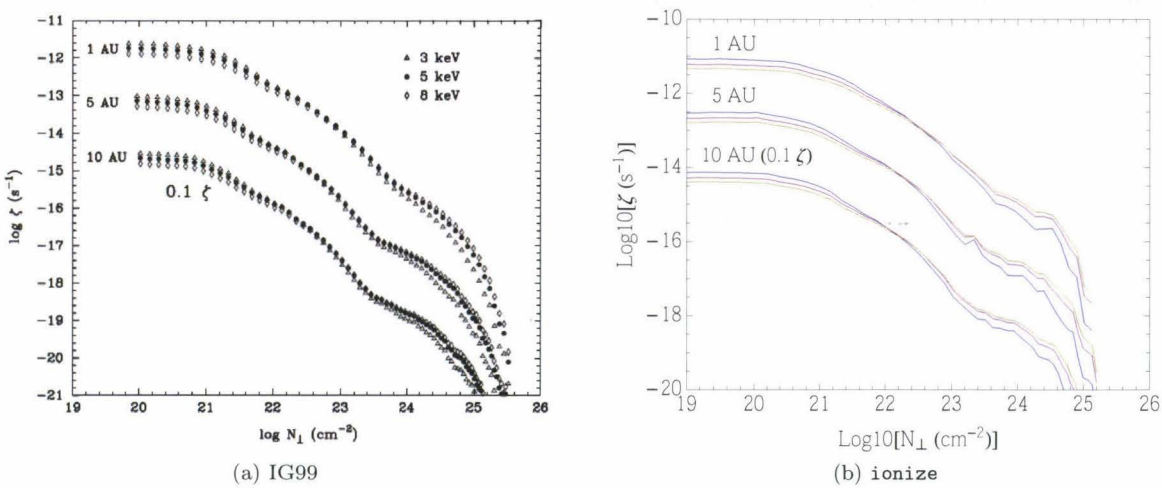

(a) IG99 (b) `ionize`

Figure 2.5: Ionization rates for the MMSN assuming a thermal x-ray spectrum, calculated using (a) IG99 for x-ray temperatures $T_X = 3$, 5, and 8 keV and (b) `ionize` for $T_X = 3$ (purple), 5 (pink), and 7 (yellow) keV. Note that in both figures, the plotted ionization rates at 10 AU were lowered by a factor of 10 for clarity. The thermal ionization rates calculated via `ionize` are greater than those computed by IG99 by about a factor of 2-3.

Chapter 3

Gas-Magnetic Coupling

3.1 Calculating the ionization state

Charge densities are not determined by the ionization rate alone. Positive ions created by ionizing particles can recombine with liberated electrons, and charges can aggregate on certain particles. In order to account for the redistribution of charges, a series of kinetic equations describing the chemical reactions involving charge transfer must be solved. As the rates at which the chemical reactions relevant in protostellar disks occur vary by several orders of magnitude (see Table 3.1), these equations define a set of stiff differential equations.

There are a variety of chemical reaction networks of varying complexity that have been developed. We adopt a simplified network constructed by IN06 (their model 4, see also Landry et al. (2013)) that treats the gas phase chemistry as well as gas-grain reactions. Submicron grains (inferred to exist in protostellar disks from infrared observations) can drastically reduce the ionization fraction in disks (Ilgner & Nelson, 2006, hereafter IN06). The network contains 2 elements, molecular hydrogen and magnesium, and grains with charges up to ± 2, for a total of 12 species (H_2, H_2^+, Mg, Mg^+, e^-, grains (g) with H_2 adsorbed, grains with Mg adsorbed, g, $g^{\pm}$, and $g^{\pm 2}$). This results in a total of 24 reactions, including gas-phase and gas-grain chemistry.

A brief overview of the gas phase chemistry is presented here, following the discussion in Landry et al. (2013). The gas phase chemistry is based on the reactions

$$
\begin{aligned}
H_2 &+ X \rightarrow H_2^+ + e \\
H_2^+ &+ H_2 \rightarrow H_3^+ + H \\
H_3^+ &+ CO \rightarrow HCO^+ + H_2 \\
2H &+ G \rightarrow H_2 + G \\
HCO^+ &+ e \rightarrow CO + H \\
HCO^+ &+ M \rightarrow M^+ + CO + H \\
M^+ &+ e \rightarrow M.
\end{aligned}
$$

X denotes an ionizing particle, g a grain, HCO^+ a representative molecular ion, and M a metal ion. The reactions that produce ions and electrons produce a net reaction

$$2H_2 + 2X + 2CO \rightarrow H_2 + 2HCO^+ + 2e^-. \tag{3.1}$$

These reactions are simplified to

$$\begin{aligned} H_2 &+ X &&\rightarrow HCO^+ &&+ e \\ HCO^+ &+ e &&\rightarrow H_2 \\ HCO^+ &+ Mg &&\rightarrow M^+ &&+ H_2, \end{aligned}$$

approximating the molecular ion as containing two hydrogen atoms and neglecting the reactions involving CO, which is justified as both HCO^+ and CO are much less abundant than H_2. These three reactions, in addition to 3.1, comprise the simplified network. The reaction rates assumed for each of these reactions are shown in Table 3.1.

The set of ordinary differential equations describing the chemical reaction network was integrated to equilibrium, assuming that the disk was initially neutral. The widely differing reaction rates of the chemical reaction network we consider becomes problematic when integrating their corresponding kinetic equations by explicit integration methods, for the minimum timestep required by these methods to produce a stable solution is limited by how quickly the fastest reaction proceeds. Implicit methods, and in particular the semi-implicit extrapolation method, which employs implicit differencing in discretizing the differential, allows us to overcome this difficulty by allowing large step sizes to be taken yet maintaining stability Press et al. (1992). A pre-existing solver written by N. J. Turner was used to perform this calculation.

We note that sub-micron sized grains have surface areas large enough to accomodate several additional charges; to treat them properly requires tens or hundreds additional reactions to the network. It was found, however, that in the vicinity of the planet, most grains are neutral or singly charged (i.e. there are more grains than free electrons), while in the disk atmosphere, where higher ionization rates produces a higher abundance of multiply charged grains, the Ohmic and ambipolar diffusivities (see Section 3.2) are not affected due to their dependence on the more abundant electrons and ions. The addition of grains with more than 2 charges was therefore deemed unnecessary.

Table 3.1: Gas phase chemistry and rate coefficients

Reaction		Rate Coefficient
H_2	$\rightarrow H_2^+ + e^-$	ζ
$H_2^+ + e^-$	$\rightarrow H_2$	$\tilde{\alpha} = 3 \times 10^{-6}/\sqrt{T}$ cm^3 s^{-1}
$M^+ + e^-$	$\rightarrow M + h\nu$	$\tilde{\gamma} = 3 \times 10^{-11}/\sqrt{T}$ cm^3 s^{-1}
$H_2^+ + M$	$\rightarrow H_2 + M^+$	$\tilde{\beta} = 3 \times 10^{-9}$ cm^3 s^{-1}

3.2 Conditions for coupling the gas to the magnetic field

Magnetic fields couple to charged particles, possibly influencing the particle's dynamics. In partially ionized environments such as the protostellar disk, the magnetic fields may not couple as effectively to the surrounding fluid, causing the magnetic field to "slip" or diffuse through the partially ionized material without affecting its dynamics. In the context of the formation of giant planets, gas accreting onto the planet may raise magnetic forces high enough to halt further accretion and truncate growth – if the flow is ionized well enough to convserve mangetic flux.

The degree to which the magnetic field couples to the surrounding material is described by the magnetic diffusivity. In the context of the potostellar disk, the diffusivity results from the collision of charge carriers with the prevailing neutrals, giving rise to non-ideal effects. The change in the magnetic field including these nonideal terms is described by the MHD induction equation

$$\frac{\partial \boldsymbol{B}}{\partial t} = \nabla \times (\boldsymbol{v} \times \boldsymbol{B}) - \nabla \times [\eta_O \nabla \boldsymbol{B} + \eta_H (\nabla \times \boldsymbol{B}) \times \hat{\boldsymbol{B}} + \eta_A (\nabla \times \boldsymbol{B})_\perp], \tag{3.2}$$

where η_O, η_H, and η_A are the ohmic, Hall, and ambipolar diffusivities, respectively. The ohmic diffusion describes changes in the field due to the dissipation of current via collisions, while the Hall diffusivity describes the generation of current due to the movement of charged particles at an angle to the field, and the ambipolar diffusivity arises due to the movement of neutrals relative to charged particles.

Wardle (2007) calculated the magnetic diffusivity by first considering the drift of charged species when an electric field $\boldsymbol{E}'$ is applied to derive the current density, given by

$$\boldsymbol{J} = \sigma_O \boldsymbol{E}'_\parallel + \sigma_H \hat{\boldsymbol{B}} \times \boldsymbol{E}'_\perp + \sigma_P \boldsymbol{E}'_\perp \tag{3.3}$$

where the ohmic, Hall, and Pederson conductivities are, respectively,

$$\sigma_O = \frac{ec}{B} \sum_j n_j |Z_j| \beta_j, \tag{3.4}$$

$$\sigma_H = -\frac{ec}{B} \sum_j \frac{n_j Z_j}{1 + \beta_j^2}, \tag{3.5}$$

$$\sigma_P = \frac{ec}{B} \sum_j \frac{n_j |Z_j| \beta_j}{1 + \beta_j^2}. \tag{3.6}$$

Solving for the induction equation gives the ohmic, Hall, and ambipolar diffusivities,

$$\eta_O = \frac{c^2}{4\pi\sigma_O}, \tag{3.7}$$

$$\eta_H = \frac{c^2}{4\pi\sigma_\perp}\frac{\sigma_H}{\sigma_\perp}, \tag{3.8}$$

$$\eta_A = \frac{c^2}{4\pi\sigma_\perp}\frac{\sigma_P}{\sigma_\perp} - \eta_O, \tag{3.9}$$

where $\sigma_\perp = \sqrt{\sigma_H^2 + \sigma_P^2}$.

If the diffusivity is sufficiently high, magnetic fields will slip quickly out of the material and thus have no effect on the dynamics of the fluid. By dimensional arguments, one can construct the dimensionless coupling condition from 3.2,

$$R_M = \frac{Lv}{\eta}, \tag{3.10}$$

i.e. the magnetic Reynolds number, where L and v are the characteristic length and velocity of the fluid, respectively. For a gas to be well-coupled to the magnetic field, $R_M \gg 1$; for an infinitely conducting fluid, $R_M = \infty$. In the protostellar context, the weakest condition for coupling is that the field at radius R couples to the Keplerian shear within one orbital period, i.e.

$$R_M = \frac{R^2\Omega}{\eta}. \tag{3.11}$$

where $\Omega = (GM_*/R^3)^{1/2}$ is the orbital angular velocity at radius R. A second condition, the Elsasser number, traces the locations where coupling is sufficient to support turbulence, and is given by

$$\Lambda = \frac{v_A^2}{\eta\Omega}, \tag{3.12}$$

where $v_A = B/4\pi\rho$ the the Alfvén speed. Turbulence occurs if $\Lambda > 1$.

Chapter 4

The Formation of Saturn

4.1 Disk Structure

The proto-Saturn was sufficiently massvie for the torques it exerted on the surrounding protosolar disk to open a gap. The gapped disk model we used was obtained from Lubow & D'Angelo (2006), in which the surface density profile of a disk with an accreting protoplanet was derived by balancing the gap-opening planetary torques with gap-closing viscous forces. The gap was placed at 10 AU, the current location of Saturn, and assumed a viscous stress parameter of α=0.005, a planetary accretion efficiency $E = 6$ (correponding to an accretion rate onto the planet of $\sim 10^{-3} M_p$ yr^{-1}), a gap width parameter $f = 2$, and a planet to star mass ratio of $q = 10^{-4}$. The surface density was scaled so that the mass of the disk (integrated from about 0.04 to 40 AU) would not exceed 0.1 $M_\odot$, above which the disk is susceptible to fragmentation under its own self-gravity. The resulting surface density profile is shown in Figure 4.1a, which produces a disk mass of 0.066 $M_\odot$, a factor of a few times more massive than the MMSN (e.g. Chiang & Youdin (2010)).

The presence of a gap introduces modifications to the disk structure caused by heating of the exposed outer wall of the gap. As the outer wall is directly illuminated, it heats and expands in order to maintain hydrostatic equilbrium. This allows the rim to intercept greater amounts of starlight, resulting in more heating and expansion, eventually causing the rim to "puff up". The material directly behind the rim is shadowed, and thus becomes cooler and contracts. Thus in order to obtain a self-consistent vertical density profile that accounts for these radiative effects, we computed optical and infrared radiative transfer and hydrostatic equilbrium as described in Section 2.2, iterating between the two five times to convergence. The proto-Sun was assumed to be of solar radius ($R_\odot = 7 \times 10^{10}$ cm) and emit at solar luminosity ($L_\odot = 4 \times 10^{33}$ erg s^{-1}). This fixes the effective protosolar temperature to be about 5800 K. The solar luminosity was divided into 10^7 photon packets. The disk was gridded into 120 logarithmically-spaced cells in radius and 60 cells in the vertical direction, spanning 0.04 to 40 AU and 6 pressure scale heights in each dimension, respectively.

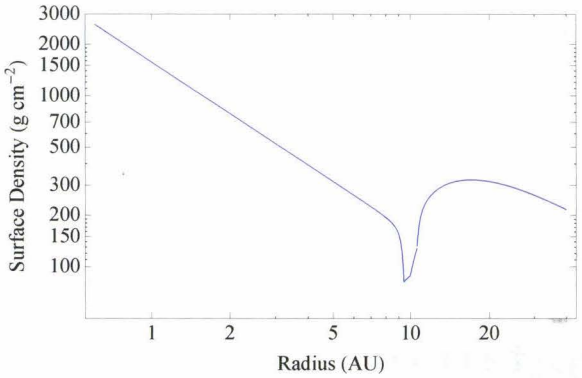

(a) Surface density profile accounting for Saturn's torques.

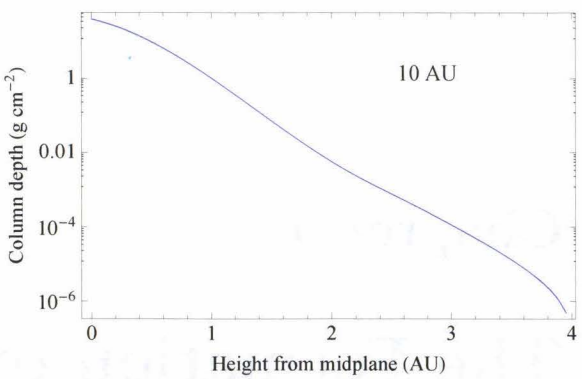

(b) Mapping of column depth to height at 10 AU.

Figure 4.1: (a) Gapped surface density profile that takes into account the torques on the disk due to the forming planet and the restoring viscous forces, derived by Lubow & D'Angelo (2006). The gap was placed at 10 AU, the current location of Saturn. (b) The column depth with height at 10 AU. The density closely follows a gaussian both in the isothermal interior and optically thin disk surface. Temperatures changes in the interveing region causes the column depth to depart from the gaussian.

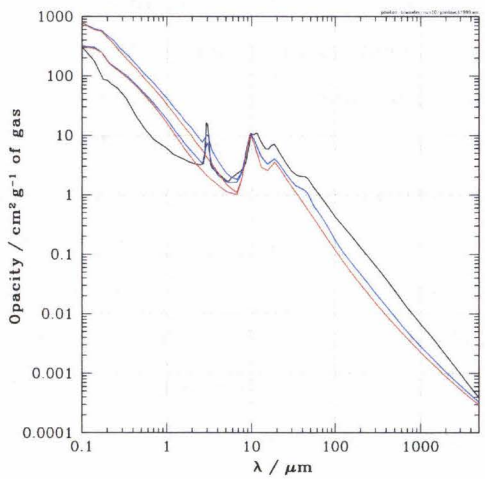

Figure 4.2: Optical and infrared dust opacities, derived from Preibisch et al. (1993). The opacities relevant to this study are in red (grains without an icy mantle), and blue (grains with a mantle). The lower curves denote the absorption opacity, while the upper curve denote the total opacity, including scattering.

Our grain model was taken from Preibisch et al. (1993), which assumes that the disk is of solar composition and that the grains follow the particle size distribution

$$n(a) \propto a^{-q}, \qquad a_{min} < a < a_{max}. \tag{4.1}$$

At temperatures below 125 K, the model assumes that grains are composed of a silicate core and an icy mantle polluted with grains of amorphous carbon ($a_{min} = 0.007\mu$m, $a_{max} = 0.03\mu$m). Above 125 K, the icy mantle sublimates, baring a silicate grain ($a_{min} = 0.04\mu$m, $a_{max} = 1\mu$m) and releasing the amorphous carbon grains; the silicates sublimate at 1500 K, and the carbon grains sublimate at 2000 K. All grains are assumed to follow a size distribution that scales with the particle size as $q = 3.5$. Scattering was assumed to be isotropic. The opacities corresponding to this grain model are shown in Figure 4.2.

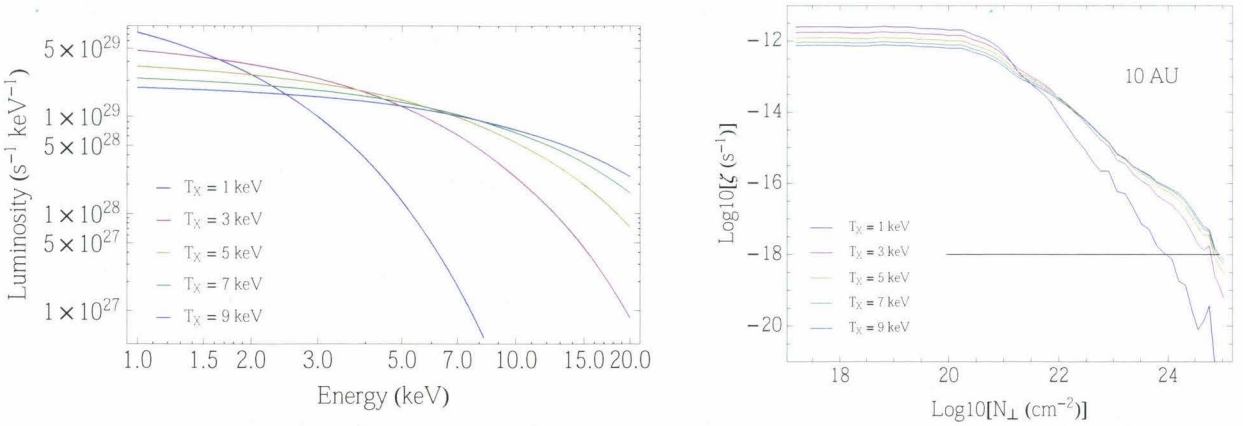

(a) X-ray source spectra.

(b) Ionization rates at 10 AU assuming a thermal x-ray spectrum.

Figure 4.3: (a) Thermal bremsstralung x-ray spectrum assuming that a plasma temperature of 1, 3, 5, 7, and 9 keV. (b) Ionization rates at 10 AU assuming a thermal x-ray spectrum. The horizontal black line denotes the ionization rate of cosmic rays, which we have assumed to be 10^{-18} s^{-1}. At lower x-ray temperatures, more softer x-rays are produced. Softer x-rays do not penetrate as deeply into the disk compared to harder x-rays due to their low albedos (see Fig. 2.2), so lower temperature sources ionize the disk surface most effectively while ionizing the disk interior the least effectively. Ionization rates at the midplane for each of the source spectra are 9×10^{-24} s^{-1}, 6×10^{-20} s^{-1}, 3×10^{-19} s^{-1}, 6×10^{-19} s^{-1}, and 7×10^{-19} s^{-1}, respectively (in order from coolest to hottest sources).

4.2 X-ray Transfer

Ionization rates were calculated by performing x-ray transfer on the resultant disk model, again assuming solar abundances of heavy elements (i.e. $\epsilon = 1$ for the opacities given in Bethell & Bergin (2011)), though heavy elements may settle onto dust grains as grains condense and begin to grow. We considered five x-ray source temperatures ranging from T_X 1 to 9 keV and an x-ray luminosity of $L_X = 2 \times 10^30$ erg s^{-1} (see Figure 4.3). Following IG99, we adopt a low-energy cut-off at 1 keV due to attenuation of low energy x-rays by the protosolar wind.

The protosolar wind was likely emitted in a bipolar conical configuration as is observed in young stars. At the distance of Saturn, some cosmic rays may be able to slip beneath this wind and reach the disk. We thus adopt a constant cosmic ray ionization rate of 10^{-18} s^{-1}, an order of magnitude less than interstellar rate to account for the wind at 10 AU.

X-ray transfer was performed with 10^5 packets for each of 20 monochromatic x-ray energies ranging between 1 - 20 keV. Thermal ionization rates were constructed by the weighting procedure described in 2.2 for each of the x-ray source temperatures we considered. The ionization rates at 10 AU are shown in Figure 4.3b. For all x-ray sources, ionization rates are constant throughout the optically thin disk surface, where the rate is determined by the flux of low energy x-rays. At higher column densities, the disk begins to become optically thick to softer x-rays, precipitating a sharp decline in ionization rate. As higher temperature sources emit more high-energy x-rays that

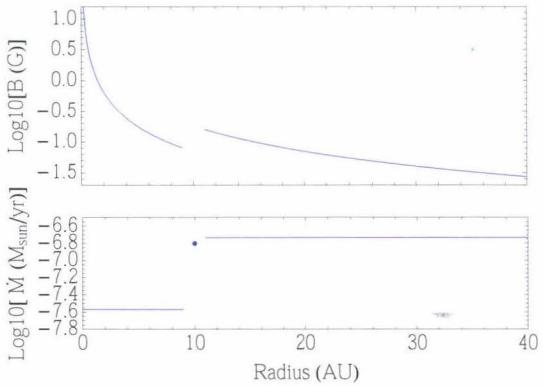

Figure 4.4: Magnetic field strengths (top), and accretion rates (bottom) for the disk. Field strengths represent a lower bound for the RMS field assuming an optimum magnetic field orientation. Accretion onto the planet causes the accretion rate interior to the gap to drop, producing a corresponding drop in the magnetic field interior to the planet's orbit. The point denotes the accretion rate at the location of the planet.

can penetrate deeper into the disk, they produce higher ionization rates. The higher-temperature ionization rates also exhibit a shoulder at a column depths greater than $N_H = 10^{23}$ cm^{-2}, where high-energy x-rays, which have a high albedo, were scattered into the disk interior.

X-ray ionization rates at the midplane range from as low as 10^{-23} s^{-1} for $T_X = 1$ keV and up to $t \times 10^{-19}$ s^{-1} for $T_X = 9$ keV. The ionization due to cosmic rays dominates at this depth. For the following analyses, we assumed that the x-ray source had a temperature of 5 keV.

4.3 Gas-magnetic coupling

To calculate magnetic diffusivities, two different dust-to-gas mass ratios were modeled, one assuming that no growth of grains, with a dust-to-gas mass ratio of 0.01, and one assuming that most of the small grains had aggregated into solid bodies, corresponding to a dust-to-gas mass ratio of 10^{-4}. Grains were assumed to have a radius of 0.1 μm and a density of 2 g cm^{-3}, which reproduces the geometric cross section per unit mass for interstellar grains. The metal ion in the chemical network was assumed to be magnesium, with a solar abundance of $3.39 \times 10^5 n_H$.

We estimated field strengths beyond and before the gap to derive upper and lower bounds for the field near proto-Saturn. As mentioned in Section 1.2, the magnetic field scales with the local accretion rate and distance from the central protostar. The accretion rates inside and outside the planet's orbit, calculated as given in Lubow & D'Angelo (2006), are 2.7 $\times 10^{-8}$ and 1.8 $\times 10^{-7}$ M$_\odot$ yr^{-1}. Applying equation 1.1, we obtain lower bounds on the field strengths of 0.08 and 0.16 G at 1 AU before and beyond the gap. We therefore considered field strengths of 0.1 G as well as a slightly stronger field of 1 G.

Diffusivities are sufficiently low for the material around proto-Saturn to satisfy the shear coupling condition if the dust mass fraction is 10^{-4}. For all other models, both the turbulent and shear coupling conditions are not fulfilled. The ambipolar diffusivity dominates the overall diffusivity throughout the height of the disk, with the main contribution due to molecular ions. The magnitude of the Hall diffusivity about equals or exceeds the ambipolar diffusivity in the disk interior and is

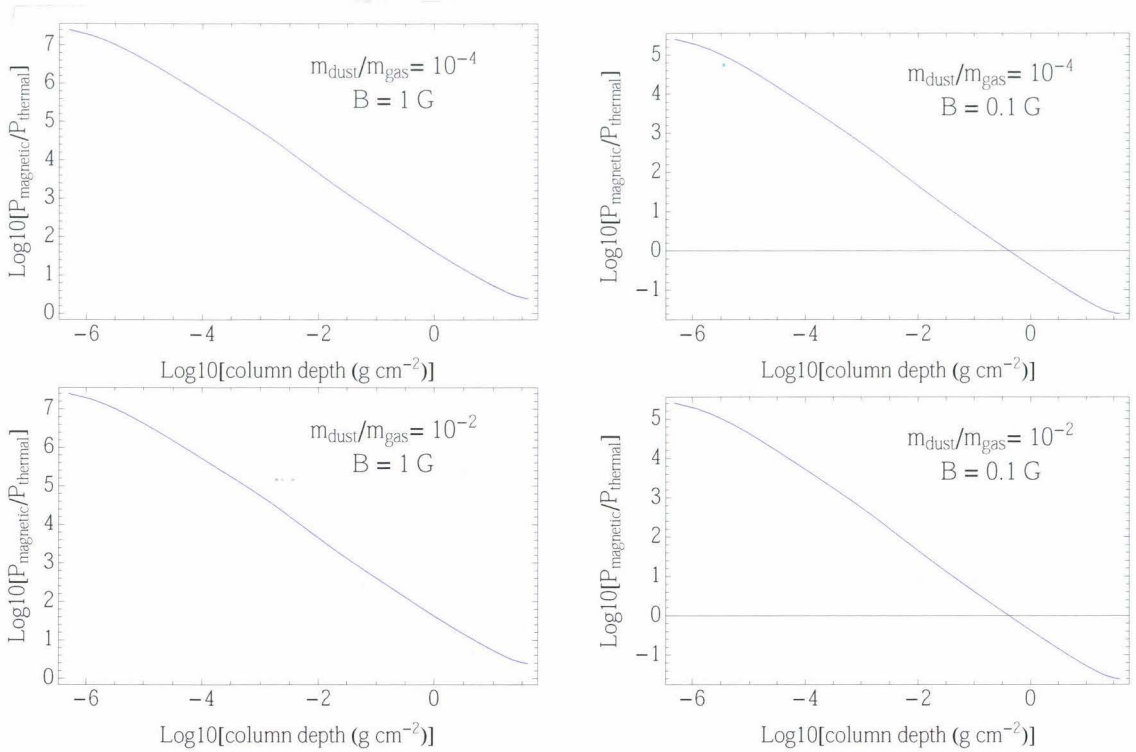

Figure 4.5: Ratio of the magnetic to the gas thermal pressure at 10 AU. In order for MRI turbulence to develop, the gas thermal pressure must exceed the magnetic pressure. This is only satisfied close to the disk midplane.

typically negative, but we ignore its contribution as the Hall effect has not been shown to produce significant effects on gas dynamics. Notably, for all field strengths and dust mass fractions, the coupling conditions are fulfilled at intermediate column depths, producing Elsasser numbers as high as $\Lambda_{\max} = 10$ - 100 and Reynolds numbers as high as $R_{M,\max} = 100$ at their peaks. The coupling parameters dip down below the threshold for coupling at the disk surface, where the so densities are low that collisions occur too rarely to tie the neutrals to the plasma.

The Elsasser and magnetic Reynolds numbers at intermediate column depths appear promising for the development of turbulence, which may be able to affect the conditions near the vicinity of the planet. However, the fulfillment of the coupling criteria do not directly entail the development of turbulence. A linear analysis by Kim & Ostriker (2000) demonstrated that growth of shear and buoyancy instabilities goes to zero when the ratio of the magnetic pressure to the gas pressure does to infinity, given that the toroidal component of the magnetic field is significant (as it usually is in 3D simulations). As shown in Figure 4.5, the gas pressure is greater than the magnetic pressure only at column depth of about 1 g cm^{-3} or greater if the field strength is 0.1 G, and is never achieved if the field is 1 G.

We note that the length of time it takes for the chemical species to reach their equilbrium concentrations exceed the orbital period of Saturn throughout the height of the disk, with longer

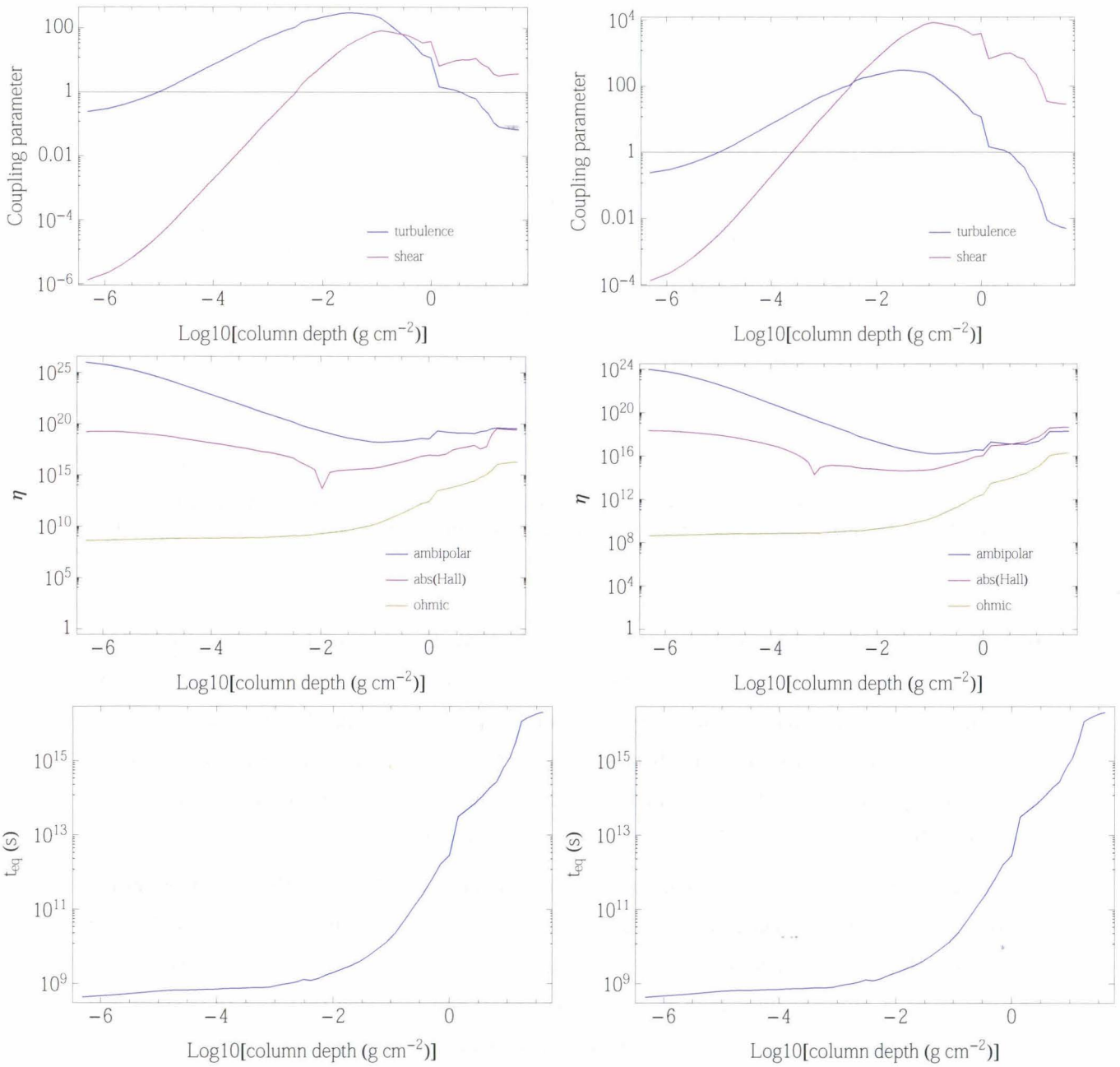

Figure 4.6: Coupling parameters, magnetic diffusivities, and time it takes to reach equilibrium at 10 AU, assuming that dust has grown (i.e. the dust to gas mass ratio is 10^{-4}) and that the disk is threaded with a field of 1 G (right) and 0.1 G (left)

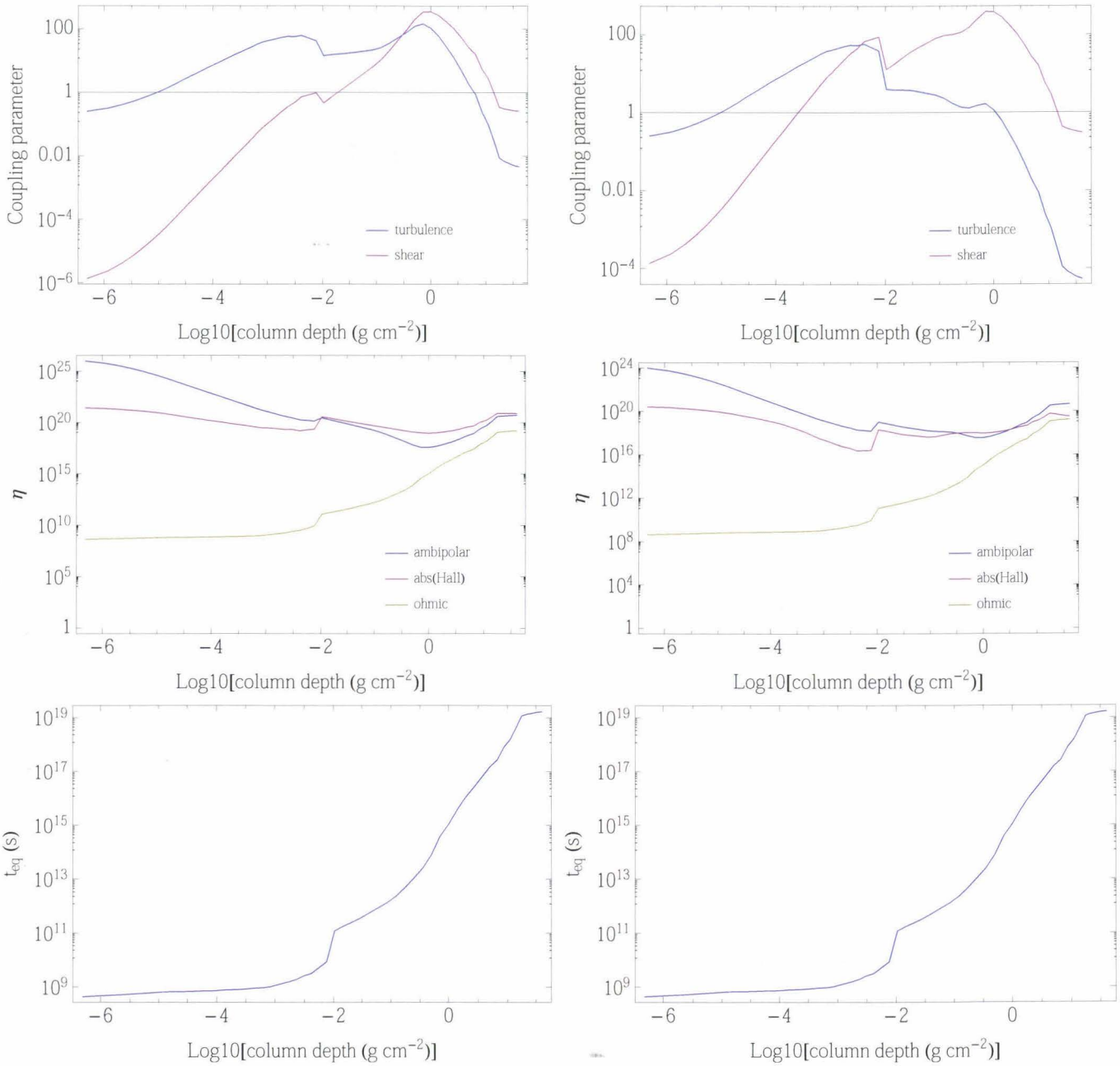

Figure 4.7: Coupling parameters, magnetic diffusivities, and time it takes to reach equilibrium at 10 AU, assuming that small grains has not been incorporated into larger solid bodies (i.e. the dust to gas mass ratio is 10^{-2}) and that the disk is threaded with a field of 1 G (right) and 0.1 G (left)

equilbrium timescales deeper into the disk. At the midplane, the timescale to reach equilibrium exceeds the disk lifetime (which is on the order of 10^6 years). The dependence on height derives from the decreasing abundance of charged species deeper in the disk. The long timescales imply that number densities are likely to be in disequilibrium.

Chapter 5

Conclusions

In order to determine whether magnetic fields had a role in truncating the growth of proto-Saturn and preventing it from reaching masses comparable to Jupiter's, as predicted by the core-accretion model of giant planet formation, a Monte Carlo radiative transfer code for protostellar disks was extended to compute x-ray transfer. The ionization rates produced by the x-rays were inputted into a chemical reaction network, which was solved to determine the ionization state of the disk. Magnetic diffusivities of the gas in the disk were then computed, from which the extent of the gas-magnetic coupling were inferred.

We have shown for field strengths of 1 G, linear shear and buoyant instabilities will likely not develop appreciably in the vicinity of proto-Saturn as the magnetic pressure exceeds the gas thermal pressure. For a field strength of 0.1 G, the gas pressure dominates at depths of $\sim$1 g cm^{-2} or greater. At these depths, the magnetic field is well-coupled to the shear in the vicinity of Saturn if the dust to gas mass ratio has been decreased to 10^{-4} (e.g. through the incorporation of grains into solid bodies). At a height of $\sim$1 g cm^{-2} (about twice Saturn's Hill radius), MRI turbulence may be able to develop as well. For a solar dust to gas mass ratio, the magnetic field is coupled to the shear above $\sim$0.5 g cm^{-2} and marginally coupled for the development of turbulence at about $\sim$1 g cm^{-2}.

While the gas-magnetic coupling may not be strong enough to allow the MRI to grow quickly near the vicinity of the proto-Saturn, the development of the instability at intermediate layers could potentially affect the gas flow near the planet and affect its accretion rates. Moreover, non-linear instabilities could develop in the transition region between the magnetic pressure dominated atmosphere and the gas pressure dominated disk interior, as demonstrated by Miller & Stone (2000). It appears that magnetic fields may have a role in gas dynamics near proto-Saturn, but a full treatment of the magnetohydrodynamics is required in order to determine specific outcomes and more securely establish whether the influence of magnetic fields can explain Saturn's low mass.

Bibliography

Armitage, P. J. 2010, Astrophysics of Planet Formation

Bai, X.-N., & Goodman, J. 2009, ApJ, 701, 737

Bethell, T. J., & Bergin, E. A. 2011, ApJ, 740, 7

Bjorkman, J. E., & Wood, K. 2001, ApJ, 554, 615

Chiang, E., & Youdin, A. N. 2010, AREPS, 38, 493

Howard, A. W., Marcy, G. W., Bryson, S. T., et al. 2012, ApJS, 201, 15

Hubickyj, O., Bodenheimer, P., & Lissauer, J. J. 2005, Icarus, 179, 415

Igea, J., & Glassgold, A. E. 1999, ApJ, 518, 848

Ilgner, M., & Nelson, R. P. 2006, A&A, 445, 205

Kim, W.-T., & Ostriker, E. C. 2000, ApJ, 540, 372

Landry, R., Dodson-Robinson, S. E., Turner, N. J., & Abram, G. 2013, ArXiv e-prints

Lissauer, J. J., & Stevenson, D. J. 2007, Protostars and Planets V, 591

Lubow, S. H., & D'Angelo, G. 2006, ApJ, 641, 526

Lucy, L. B. 1999, A&A, 344, 282

Miller, K. A., & Stone, J. M. 2000, ApJ, 534, 398

Pollack, J. B., Hubickyj, O., Bodenheimer, P., et al. 1996, Icarus, 124, 62

Preibisch, T., Ossenkopf, V., Yorke, H. W., & Henning, T. 1993, A&A, 279, 577

Press, W. H., Teukolsky, S. A., Vetterling, W. T., & Flannery, B. P. 1992, Numerical recipes in C. The art of scientific computing

Turner, N. J., Choukroun, M., Castillo-Rogez, J., & Bryden, G. 2012, ApJ, 748, 92

Turner, N. J., & Sano, T. 2008, ApJL, 679, L131

Umebayashi, T., & Nakano, T. 1981, PASJ, 33, 617

Wardle, M. 2007, Ap&SS, 311, 35